Robust Si/Ge heterostructure metasurfaces as building blocks for wavelength-selective photodetectors EP

iD J. Schlipf, iD F. Berkmann, iD Y. Yamamoto, et al.

COLLECTIONS

EP This paper was selected as an Editor's Pick

View Online   Export Citation   CrossMark

ARTICLES YOU MAY BE INTERESTED IN

Magnetoplasmonics in confined geometries: Current challenges and future opportunities
Applied Physics Letters **122**, 120502 (2023); https://doi.org/10.1063/5.0136941

Electrode pattern definition in ultrasound power transfer systems
Applied Physics Letters **122**, 124101 (2023); https://doi.org/10.1063/5.0139866

Silver-decorated cobalt–molybdenum oxide nanosheets as a pH-universal electrocatalyst for high-efficiency hydrogen evolution reaction
Applied Physics Letters **122**, 123906 (2023); https://doi.org/10.1063/5.0139102

AIP Publishing

Robust Si/Ge heterostructure metasurfaces as building blocks for wavelength-selective photodetectors

J. Schlipf,[1,a] F. Berkmann,[2] Y. Yamamoto,[3] M. Reichenbach,[4] M. Veleski,[4] Y. Kawaguchi,[2] F. Mörz,[5] J. W. Tomm,[6] D. Weißhaupt,[2] and I. A. Fischer[1]

AFFILIATIONS

[1]Chair of Experimental Physics and Functional Materials, BTU Cottbus-Senftenberg, Cottbus, Germany
[2]Institute for Semiconductor Engineering (IHT), University of Stuttgart, Stuttgart, Germany
[3]IHP-Leibniz-Institut für Innovative Mikroelektronik, Frankfurt, Germany
[4]Chair of Computer Engineering, BTU Cottbus-Senftenberg, Cottbus, Germany
[5]4th Physics Institute, University of Stuttgart, Stuttgart, Germany
[6]Max-Born-Institute for Nonlinear Optics and Short Pulse Spectroscopy, Berlin, Germany

a)Author to whom correspondence should be addressed: schlipf@b-tu.de

ABSTRACT

We present a design for silicon-compatible vertical Germanium pin photodiodes structured into all-dielectric metasurfaces. Proof-of-principle metasurfaces are fabricated on silicon-on-insulator wafers in a top-down process. Simulations and measurements of the spectroscopic properties, specifically the absorption, show high spectral selectivity, and absorption efficiencies as large as those in bulk Germanium layers with about four times the Ge layer thicknesses. Our metasurface structures can be tuned to the target wavelength through tailoring of the lateral geometry. Possible applications include spectroscopy and hyperspectral imaging, with several metasurfaces for different wavelength ranges integrated with readout circuitry into a low-cost electronic–photonic integrated circuit.

Optical metasurfaces consisting of two-dimensional arrangements of sub-wavelength sized metallic or dielectric nanostructures can be used to manipulate light properties in layers with sub-wavelength thicknesses.[1–4] Optical metasurfaces have been conceived to function as perfect[5] and selective[5,6] absorbers and lenses.[7] Possible applications of optical metasurfaces include their use as filters in combination with CMOS image sensors[8] or as building blocks for biosensors.[9,10] Comparatively, few attempts have been made to incorporate metasurfaces directly into optoelectronic devices and make use, e.g., of their wavelength-selective and polarization-selective properties. Metallic metasurfaces have been combined with bulk photodetectors for photocurrent enhancement and sensing.[11,12] Dielectric metasurfaces have been structured into the top layer of both bulk Si and Ge photodiodes for broadband responsivity enhancement.[13]

Incorporating metasurfaces directly into optoelectronic devices is challenging because of the need for contacting of the elements of the metasurface as well as increased fabrication complexity. While metasurface devices with individual electrical contacts to the nanostructured elements of the metasurface have been proposed based on simulations,[14] those are difficult to realize experimentally, and contacting schemes based on the introduction of continuous layers connecting all metasurface elements are preferred from a device fabrication point of view. However, the presence of those layers can affect the electromagnetic field distribution within the device and possibly degrade optical properties.

Here, we investigate a metasurface design for incorporation into a photodetector that not only features narrow bandwidth absorption but is also robust with respect to variations in fabrication parameters. We find that using a heterostructure Si/Ge metasurface in particular is key for improving wavelength selectivity and enhancing responsivities. While the optical properties of the fabricated metasurface are degraded compared to those predicted by simulations, our fabricated metasurface, nonetheless, shows a clear absorption peak at 1405 nm with a peak absorption of 45%. Furthermore, we argue that such

metasurfaces can be the building blocks for on-chip spectrometers capable of analyzing the 1200–1550 nm wavelength range with important applications, e.g., in hyperspectral imaging for crop analysis.

Our proposed metasurface photodetector, which motivates this investigation [Fig. 1(a)], is designed around a vertical Si/Ge heterostructure PIN diode on a silicon-on-insulator (SOI) substrate whose low-refractive index buried oxide layer helps confine the electromagnetic fields within the metasurface. Only the diode's intrinsic region is composed of Ge, while the doped regions contain Si. In the targeted wavelength range of operation between 1150 and 1600 nm, all other materials except Ge are transparent, ensuring efficient light absorption and photocurrent generation only in the intrinsic Ge region. Simulations show that for wavelengths above 1.1 μm, more than 99.9% of the total absorption occurs in the Ge layer (Fig. S3). The refractive indices of the materials ($n_{Si} = 3.49$, $n_{Ge} = 4.25$, $n_{SiO2} = 1.45$, and $\varepsilon_{ZnO} = 1.93$)[15–18] are sufficiently different to confine radiation to the semiconductor layers. The high-refractive-index top Si and Ge layers are periodically patterned into mesas, forming an all-dielectric metasurface. Electrical contact for such a metasurface design is possible through the transparent conductive ZnO layer and the bottom Si layer.

While the layer thicknesses are determined during deposition, in-plane patterning allows for a multitude of possible geometries and corresponding devices with adjustable optical responsivity spectra. When producing our proof-of-principle structure as shown here, we rely on undoped materials and replace the ZnO top electrode by an SiO$_2$ layer [Fig. 1(b)]. Our simulations show that the difference in optical behavior is negligible, while fabrication is far easier.

The metasurfaces were fabricated in a top-down process. Starting from a SOI substrate with a thinned-back Si layer, 150 nm of Ge was grown epitaxially by chemical vapor deposition (CVD). Cyclic annealing was used to reduce the threading dislocation density.[19] This was followed by the deposition of 45 nm of Si. After epitaxial growth, the samples were annealed at 800 °C to improve layer quality. Layer thicknesses were measured by reflectometry.

Structuring was carried out via photolithography with a positive resist (AZ MIR 701, diluted 4:1 in ethyl lactate) and etching.

The metasurfaces were defined lithographically as square 160 × 160 μm^2 arrays. This was followed by a dry etching step in an inductively coupled plasma reactive ion etching (ICP-RIE) system. After stripping the native oxide in a five second chlorine step, the mesa was etched by HBr. The etching depth was obtained from profiler measurements (Table I). The dry etching step also removed ∼30 nm of the bottom Si layer. As we will discuss further below, this etching depth can have a large influence on the absorption spectrum of the metasurfaces. Finally, a 600 nm SiO$_2$ layer was deposited by plasma-enhanced CVD from a Tetraethyl orthosilicate precursor at 350 °C, to passivate the exposed semiconductor layers and to mitigate light scattering. A schematic cross section of two unit cells of the fabricated metasurface and an scanning electron microscopy (SEM) image after etching (taken at a sample tilt of 45°) are shown in Figs. 1(b) and 1(c), respectively.

The pitch Λ was defined by the photolithography masks and was confirmed via SEM. We also measured the diameter of the pillars from the developed photoresist prior to etching and verified that this diameter is transferred to the etched semiconductor layers. However, as can be observed from the SEM image of etched samples [Fig. 1(c)], the pillar sidewalls are not perfectly vertical. As is known from previous device fabrication processes,[20,21] the Ge layers are slightly underetched compared to the Si cap layer. Furthermore, at the bottom of the pillars, a small pedestal is formed, due to overetching. This as well as slight inhomogeneities in the pillar shapes can be expected to degrade the optical properties of the metasurface, widening resonance peaks, and decreasing their amplitude.[22]

A Bruker Vertex 80 spectrometer together with a Bruker Hyperion 2000 microscope was used to obtain reflection and transmission spectra of our samples via Fourier transform infrared (FTIR) spectroscopy. Measurements for wavelengths 1 μm ≤ λ ≤ 3 μm were carried out under vertical incidence. As a consequence of interference effects resulting from the SOI substrate as well as very low losses in the substrate bulk, extraction of the metasurface absorption from the reflection and transmission spectra of the full sample required a de-embedding approach as described in the supplementary material. In previous investigations, the absorption spectra obtained from FTIR
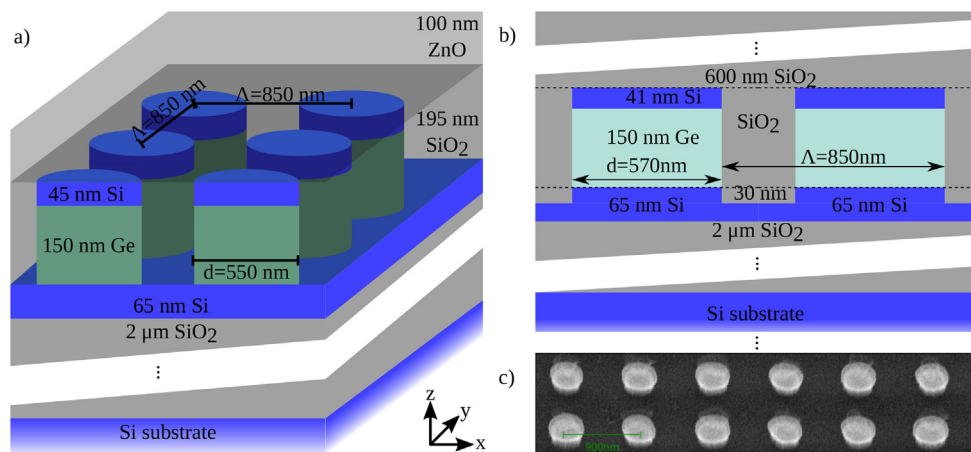
FIG. 1. (a) Metasurface photodetector device design. (b) Fabricated proof-of-principle structure. The ZnO electrode layer is replaced by SiO$_2$ for ease of fabrication. Manually controlled etching led to partial removal of the bottom Si layer. (c) SEM image of an etched sample (structure C, with a square lattice of 900 nm pitch) prior to photoresist removal, taken at a sample tilt of 45°.

TABLE I. Geometry of selected structures A to C. Measured properties are compared with values assumed in simulations to obtain a good fit to the experimental absorption spectra.

Structure	SiO$_2$ thickness t_{SiO2} (nm)	Si cap thickness t_{Si} (nm)	Ge thickness t_{Ge} (nm)	SOI-Si thickness t_{SOI} (nm)	BOX thickness t_{BOX} (nm)	Si etch depth t_{Etch} (nm)	Array pitch Λ (nm)	Pillar diameter d (nm)
Measured								
A	653	41	138	61	2005	24	850	570
B	653	41	138	61	2005	24	850	530
C	666	41	139	61	2006	18	900	340
Simulated								
A	600	45	150	64	1900	30	850	570
B	600	45	150	64	1900	30	850	520
C	600	45	150	64	1900	20	900	300

measurements combined with de-embedding approaches have been shown to be highly predictive for device responsivities.[23]

Simulations were carried out using our in-house implementation of the Rigorous Coupled-Wave Analysis (RCWA),[24] with the enhanced transmission matrix algorithm.[25] We used literature values for the optical properties of Si,[15] SiO$_2$,[18] and Ge.[16]

Here, we focus on the analysis of three different metasurface geometries (structures A, B, and C) whose absorption spectra [Figs. 2(a) and 2(b)] feature peaks, labeled with Arabic numerals, in the near infrared range.

Structures A and B have the same metasurface pitch but deviate in pillar diameter, resulting in a relative shift in the main absorption peaks at 1350 nm (structure A) and 1390 nm (structure B). Structure C features a slightly larger pitch of 900 nm, but a significantly smaller pillar diameter of 300 nm, resulting in a pronounced absorption peak at 1405 nm. We note that for wavelengths below 1200 nm, extraction of the absorption spectra from reflection and transmission measurements is no longer possible since the opaque Si substrate bulk leads to a very low transmission signal. Furthermore, peak 3 appears as a weak shoulder in the absorption spectra of structures A and B since the (direct) bandgap of Ge acts as a cutoff and causes the peak to be only partially visible.

We conducted RCWA[24] simulations of the absorption based on the measured geometry. Experiment and simulation agree qualitatively with matching resonance peaks positions under two modifications [Figs. 2(a) and 2(b)]. First, the simulations use slightly different values for the layer thicknesses and pillar diameters, in order to obtain a better fit to the experimental spectra. The layer thicknesses and in-plane geometry as measured and as used in simulations are given in Table I. Deviations in layer thicknesses can be attributed to variations in optical material parameters as well as measurement imperfections, while deviations in pillar diameters originate from imperfections in etching [Fig. 2(b)]. We note that defining pillar diameters below 500 nm lithographically is highly challenging for the mask aligner used here (Süss MA6/Gen2). A trend toward larger deviations between measured and simulated diameter can be attributed to larger fabrication imperfections in the smaller structures. Second, the absorption band edge of Ge had to be shifted by 50 nm into the infrared to obtain a better match between experimental and simulation results. This can be attributed to biaxial tensile strain introduced during the Ge growth on an SOI substrate, which is known to decrease the bandgap energy of the

material.[26] For reference, the simulated absorption in a Ge layer with a thickness of 150 nm is also shown in Fig. 2(b). In contrast to the absorption spectrum of the metasurface, the bulk absorption does not show a strong wavelength-dependence and is mainly influenced by the bandgap of the material.

Cross-sectional plots of the electric field amplitudes at the peak wavelengths are shown in Figs. 2(c)–2(f). Due to the relatively complex layer stack, the resonant modes cannot be assigned to multipole Mie or lattice resonances in most cases [e.g., mode 1, Fig. 2(c)]. Instead, they arise from hybridization of resonances of the different dielectric shapes and the lattice. One can observe the similarity in fields in the 1600 nm peak in structure A [Fig. 2(e)] and the 1405 nm peak in structure C [Fig. 2(f)]. Both correspond to mode 3, shifted to lower wavelengths due to the lower pillar diameter in structure C. Compared to simulations, the measured peaks are significantly broadened as a result of fabrication imperfections. While precision can be improved in industrial fabrication processes, it is, nonetheless, important to identify those parameters that have a particularly strong impact on peak positions and heights. Improving optical properties can then be achieved either by increasing the precision for those fabrication steps that are most relevant or, alternatively, by identifying robust metasurface geometries whose optical properties do not depend strongly on parameters that are difficult to control. We, therefore, examined the influence of variations of the four most relevant geometric parameters (array pitch Λ, pillar diameter, Ge layer thickness, and etching depth) on the absorption peaks (Fig. 3) of structure A. The peak positions were obtained from a decomposition of the spectra into a superposition of Gaussian peaks on a linear baseline, as marked in the plot. Again, we assign the corresponding resonant modes to the peaks as modes 1 to 3, consistent with the labeling in Fig. 2.

The absorption peaks show a linear dependence on the pitch Λ of the array [Fig. 3(a)]. When the peak wavelength exceeds 1600 nm, the peak is clipped by the onset of transparency related to the (direct) bandgap of Ge. Of all the parameters, Λ is the easiest to control in fabrication. However, one can observe that the shift of these peaks does not always conserve peak height. This is because the multilayer structure features several degrees of freedom, which have to be adjusted simultaneously for strong resonances.

The peak position is also influenced by pillar diameter [Fig. 3(b)] and layer thicknesses, most notably that of the absorbing Ge layer [Fig. 3(c)]. Here, the dependence of the peak position on the variable
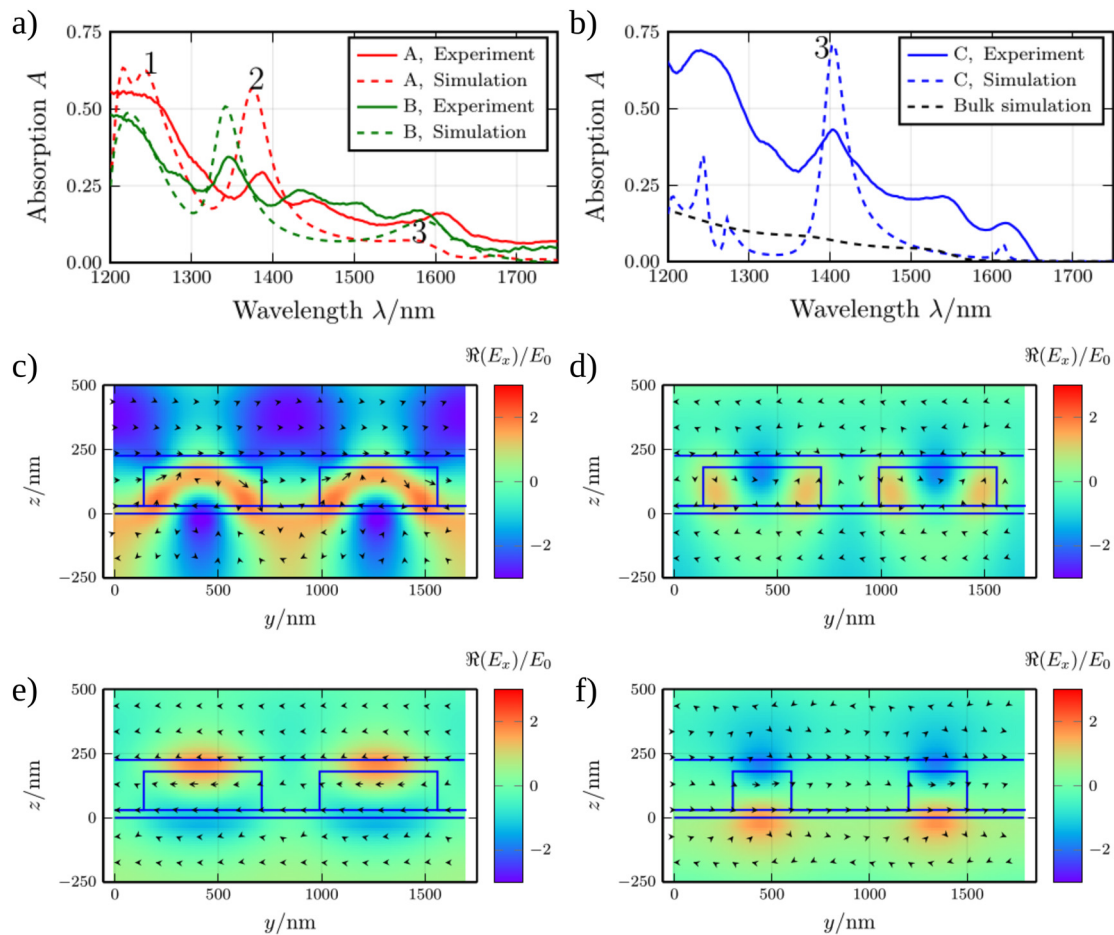
FIG. 2. (a) Extracted spectra for structures A and B compared to simulation results based on their geometric properties. The three most prominent resonant peaks are denoted with Arabic numerals. (b) Extracted and simulated absorption spectrum of structure C, compared to the expected absorption of an unstructured Ge pin photodetector. Out-of-plane electric field and in-plane magnetic field (arrows) in an x-normal cross section for (c) peak 1 of structure A, (d) peak 2 of structure A, (e) peak 3 of structure A, and (f) peak 3 of structure C.

parameter shows clear non-linearities because the peak absorption is affected by the propagation of electromagnetic waves in the continuous layers as well as in the three-dimensional cylinders. In our fabrication, we experienced deviations of up to 10% in pillar diameter, especially for smaller structures. This can lead to peak shifts by several tens of nanometers.

Finally, the etching depth in the SOI Si layer has a profound influence on mode 2 and almost none on the others [Fig. 3(d)], and mode 3 is not marked here as it is situated at the band edge [Fig. 3(e)]. This depth cannot be controlled precisely in the dry etching process that we employed, and since it can even vary over the spatial extent of the metasurface, this is a large source of potential errors. Thus, it is important to design metasurfaces to utilize a photonic mode that is robust with respect to changes in etch depth.

The robustness against the etching depth in the bottom Si layer can be understood when looking at the electric and magnetic fields in cross-sectional plots for two adjacent pillars (Fig. 2). From the three most prominent modes in structure A, the robust ones only feature a small electric field in the remaining Si. In the non-robust mode 2, the fields go through the remaining Si [Fig. 2(b)]. This makes the mode sensitive to geometry changes in this area. An increase in etch depth replaces more and more Si by SiO$_2$, which has a lower refractive index. This shortens the effective optical path lengths between the pillars and, thus, shifts the peak to a lower wavelength.

Finally, a comparison of simulated absorption spectra for a Si–Ge–Si heterostructure metasurface and a metasurface with the same geometry parameters but composed entirely of Ge [Fig. 3(f)] showcases the role of the heterostructure layers on absorption peak height and width. While the difference in refractive indices between Ge and Si is comparatively low, the presence of the Si layers below and on top of the Ge nonetheless serves to lead to stronger field confinement to the absorbing Ge, strongly increasing the height and reducing the width of the absorption peak.

Due to its robustness with respect to etching depth and the significant height of the corresponding absorption peak both in experiment and simulation, we consider mode 3 to be the most promising
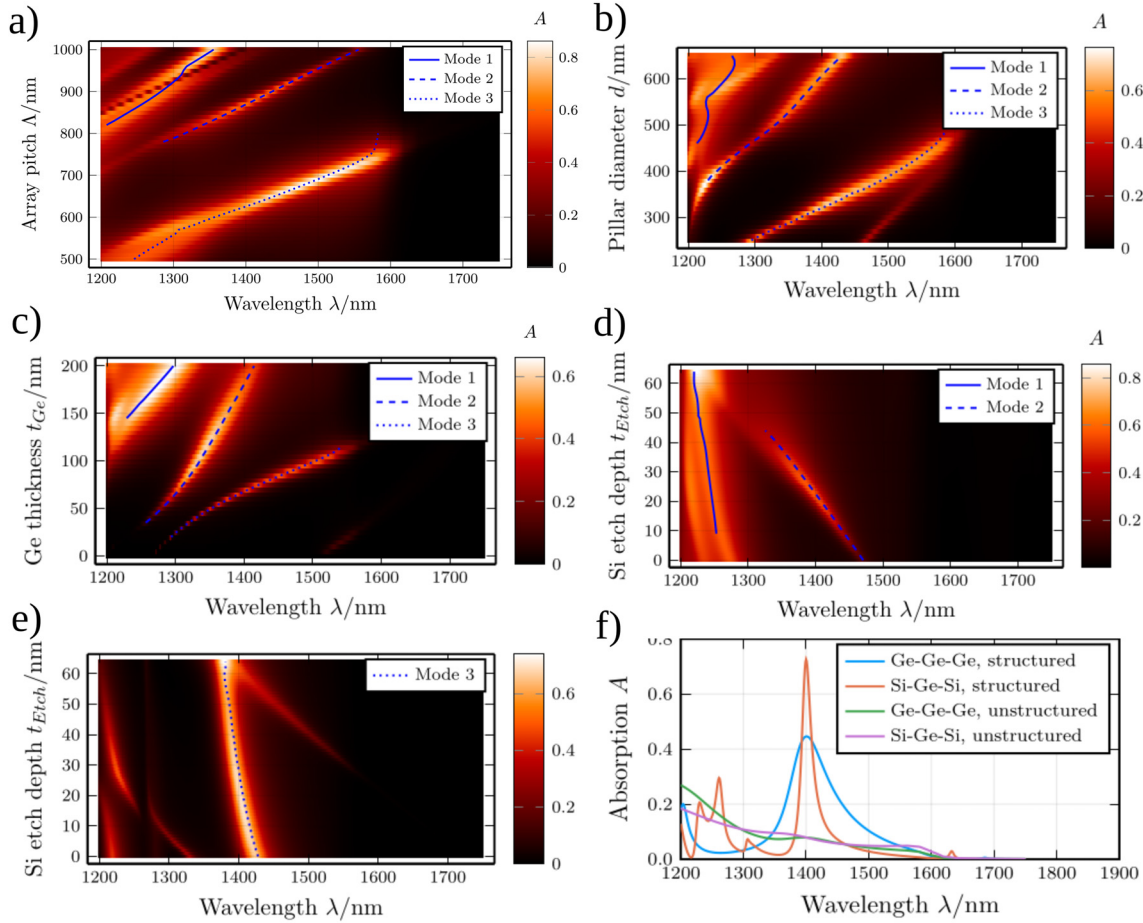
FIG. 3. (a)–(d) Absorption peak position in structure A with variation of (a) array pitch, (b) pillar diameter, (c) Ge layer thickness, and (d) Si etch depth. The default values are $\Lambda = 850$ nm, $d = 570$ nm, $t_{Ge} = 150$ nm, and $t_{Etch} = 30$ nm. (e) Shift of the absorption peak related to mode 3 in structure C. Default values are $\Lambda = 900$ nm, $d = 300$ nm, and $t_{Ge} = 150$ nm. (f) Comparison of absorption peaks in a Si–Ge–Si heterostructure compared to a pure Ge metasurface, and unstructured bulk layers of the same thickness. The geometry is identical to structure C.

candidate for a metasurface-integrated photodetector device. While the mode is present at a suitable wavelength around 1405 nm in structure C, the relatively small diameter of the Ge pillar makes fabrication challenging. It is, thus, desirable to construct a metasurface with larger pillar diameter, with the peak at the same position. Since both pitch and diameter are tunable via the photolithography mask, and their influence on the peak position is monotonic, this is feasible. We chose to optimize the structures numerically, as this can be solved as a computationally cheap single-wavelength problem, and automatic optimization easily deals with the slight nonlinearity in the relationship between peak position and pillar diameter. A very simple cost function f for optimization for maximum absorption at a given wavelength λ_m is simply the reciprocal of said absorption,

$$f(\vec{d}) = \frac{1}{A(\vec{d}, \lambda_m)}. \tag{1}$$

Here, $\vec{d}$ stands for a vector of parameter values and $A(\vec{d}, \lambda_m)$ is the absorption of a metasurface with the geometry defined by $\vec{d}$ for a

wavelength λ_m. Applying the Nelder–Mead algorithm[27] to the system with this cost function, a target wavelength $\lambda_m = 1405$ nm with the properties of structure C as starting value $\vec{d}_0$ yields a geometry with $\Lambda = 650$ nm and $d = 435$ nm. This structure can be easily tweaked through optimization for different λ_m [Fig. 4(a)]. Since this optimization conserves layer thicknesses and, thus, fabrication process parameters, it is possible to integrate multiple different metasurface photodetectors on the same integrated circuit, creating a single-shot spectrometer or hyperspectral camera.

In order to showcase the applicability of our proposed devices to spectroscopy and hyperspectral imaging, we use our simulation results [Fig. 4(a)] to examine the case of optical detection of water stress in plants based on reflection spectra of plant leaves reported in the literature[28] after different drying times and at wavelengths between 1300 and 1600 nm [Fig. 4(b)]. We assume unity conversion efficiency here, so the optical responsivity R_{opt} is the ratio of the photocurrent in the detector I divided by the incoming optical power P, which is just the absorption efficiency A divided by the photon energy,
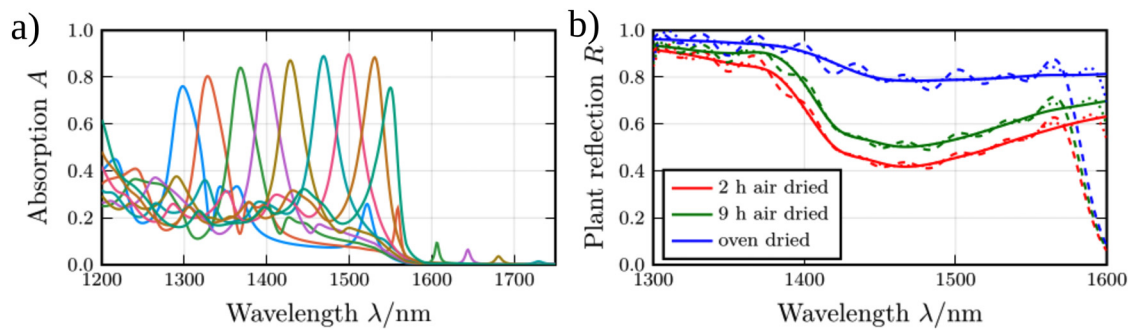
FIG. 4. (a) Selected set of nine metasurface geometries for spectral coverage between 1300 nm and 1550 nm. (b) Experimental plant reflection spectra[28] (solid lines) and reconstructed spectra for a set of 9 (dashed) or 25 (dotted, very low deviation from plant spectra) metasurface detectors. Spectra for three different sample comparisons were analyzed.

$$R_{opt}(\lambda) = \frac{I(\lambda)}{P(\lambda)} = \frac{A(\lambda)}{E_{phot}(\lambda)}. \qquad (2)$$

Since the number of different metasurface detectors employed in a spectroscopic scheme is discrete, and the optical spectrum impinging on the detector is continuous, a reconstruction algorithm is required to extract the spectral information from the measured photocurrents. An increasing number of metasurface detectors would increase reconstruction accuracy, at the cost of footprint. To solve the linear inverse problem, we chose an algorithm based on Gaussian matrices,[29,30] and a set of nine simulated metasurface photodetectors [Fig. 4(a)]. This assumes that the optical input spectrum is superposition of nine Gaussians. In matrix notation, the 9-element vector of photocurrents $\vec{i}$ is related to the 301-element vector of optical power in the input spectrum $\vec{p}$ by the 9-by-301 matrix of the photodetector responsivities R_{opt},

$$\vec{i} = R_{opt}\,\vec{p}. \qquad (3)$$

We model the spectrum by a 301-by-9 matrix G of nine Gaussian peaks with amplitudes $\vec{t}$,

$$\vec{p} \sim G\vec{t}. \qquad (4)$$

The Gaussians are equally spread within the spectral range of interest and have a standard deviation of 15 nm. One can obtain their amplitudes, and thus, an approximation of the spectrum $\vec{p}'$ from the photocurrents by solving this equation system,

$$\vec{t} = (GA)^{-1}\vec{i}, \qquad (5)$$

$$\vec{p}' = G\vec{t}. \qquad (6)$$

The results are shown in Fig. 4(b). For nine devices, the reconstructed spectrum follows the original one, but with significant deviations. While it cannot perfectly reconstruct, the scheme is sufficient to differentiate between the samples and estimate water stress.

To conclude, we present a design for all-dielectric Ge metasurfaces using Si–Ge–Si heterostructures with relatively thin Ge layers on SOI substrates for applications in optoelectronic devices. Our experimental and simulation results confirm the wavelength-selective absorption properties. We demonstrate that a simple fabrication process and the possibility of engineering for robustness against deviations in the processing parameters make our design a promising candidate for applications in spectroscopy, hyperspectral imaging, and fiber communications. Furthermore, the use, in particular, of a heterostructure metasurface design enables us to employ continuous semiconductor layers for facile electrical contacting in device applications. Thus, with few adjustments, our metasurfaces can be modified to work as wavelength-selective photodetectors on SOI substrates, compatible to a commercial Si/Ge photonics process.

See the supplementary material for details on the algorithm for the extraction of absorption spectra from measured reflection and transmission.

AUTHOR DECLARATIONS
Conflict of Interest

The authors have no conflicts to disclose.

Author Contributions

Jon Schlipf: Conceptualization (equal); Data curation (lead); Investigation (lead); Methodology (equal); Project administration (equal); Software (lead); Visualization (lead); Writing – original draft (lead); Writing – review & editing (equal). **Inga Anita Fischer:** Conceptualization (lead); Formal analysis (supporting); Investigation (equal); Methodology (equal); Project administration (equal); Resources (equal); Supervision (lead); Validation (lead); Visualization (lead); Writing – original draft (equal); Writing – review & editing (equal). **Fritz Berkmann:** Conceptualization (supporting); Investigation (equal); Methodology (supporting); Writing – original draft (supporting); Writing – review & editing (supporting). **Yuji Yamamoto:** Investigation (equal); Methodology (supporting); Writing – original draft (supporting); Writing – review & editing (supporting). **Marc Reichenbach:** Conceptualization (equal); Data curation (equal); Methodology (equal); Writing – original draft (equal); Writing – review & editing (supporting). **Mitko Veleski:** Investigation (equal); Methodology (supporting); Writing – original draft (equal); Writing – review & editing (supporting).

Yuma Kawaguchi: Investigation (supporting); Methodology (supporting). **Florian Mörz:** Methodology (supporting). **Jens W. Tomm:** Investigation (supporting); Methodology (supporting); Writing – original draft (equal); Writing – review & editing (equal). **David Weisshaupt:** Investigation (supporting).

DATA AVAILABILITY

The data that support the findings of this study are available from the corresponding author upon reasonable request.

REFERENCES

[1] L. Martín-Moreno, F. J. García-Vidal, H. J. Lezec, K. M. Pellerin, T. Thio, J. B. Pendry, and T. W. Ebbesen, "Theory of extraordinary optical transmission through subwavelength hole arrays," Phys. Rev. Lett. **86**(6), 1114–1117 (2001).

[2] H.-T. Chen, A. J. Taylor, and N. Yu, "A review of metasurfaces: Physics and applications," Rep. Prog. Phys. **79**(7), 076401 (2016).

[3] P. Genevet, F. Capasso, F. Aieta, M. Khorasaninejad, and R. Devlin, "Recent advances in planar optics: From plasmonic to dielectric metasurfaces," Optica **4**(1), 139–152 (2017).

[4] M. Chen, M. Kim, A. M. H. Wong, and G. V. Eleftheriades, "Huygens' metasurfaces from microwaves to optics: A review," Nanophotonics **7**(6), 1207–1231 (2018).

[5] W. Li, Z. J. Coppens, L. V. Besteiro, W. Wang, A. O. Govorov, and J. Valentine, "Circularly polarized light detection with hot electrons in chiral plasmonic metamaterials," Nat. Commun. **6**(1), 8379 (2015).

[6] A. Tittl, A. Leitis, M. Liu, F. Yesilkoy, D.-Y. Choi, D. N. Neshev, Y. S. Kivshar, and H. Altug, "Imaging-based molecular barcoding with pixelated dielectric metasurfaces," Science **360**(6393), 1105–1109 (2018).

[7] J. B. Pendry, "Negative refraction makes a perfect lens," Phys. Rev. Lett. **85**(18), 3966–3969 (2000).

[8] Z. Wang, S. Yi, A. Chen, M. Zhou, T. S. Luk, A. James, J. Nogan, W. Ross, G. Joe, A. Shahsafi, K. X. Wang, M. A. Kats, and Z. Yu, "Single-shot on-chip spectral sensors based on photonic crystal slabs," Nat. Commun. **10**(1), 1020 (2019).

[9] A. Krasnok, M. Caldarola, N. Bonod, and A. Alú, "Spectroscopy and biosensing with optically resonant dielectric nanostructures," Adv. Opt. Mater. **6**(5), 1701094 (2018).

[10] A. Prasad, J. Choi, Z. Jia, S. Park, and M. R. Gartia, "Nanohole array plasmonic biosensors: Emerging point-of-care applications," Biosens. Bioelectron. **130**, 185–203 (2019).

[11] A. Shakoor, B. C. Cheah, D. Hao, M. Al-Rawhani, B. Nagy, J. Grant, C. Dale, N. Keegan, C. McNeil, and D. R. S. Cumming, "Plasmonic sensor monolithically integrated with a CMOS photodiode," ACS Photonics **3**(10), 1926–1933 (2016).

[12] L. Augel, Y. Kawaguchi, S. Bechler, R. Körner, J. Schulze, H. Uchida, and I. A. Fischer, "Integrated collinear refractive index sensor with Ge PIN photodiodes," ACS Photonics **5**(11), 4586–4593 (2018).

[13] J. Song, S. Yuan, C. Cui, Y. Li, C. Zeng, and J. Xia, "Photonic crystal enabled manipulation of optical and electric field in germanium avalanche photodetectors," Nanotechnology **32**(14), 145201 (2021).

[14] R. Masoudian Saadabad, C. Pauly, N. Herschbach, D. N. Neshev, H. T. Hattori, and A. E. Miroshnichenko, "Highly efficient near-infrared detector based on optically resonant dielectric nanodisks," Nanomaterials **11**(2), 428 (2021).

[15] C. Schinke, P. Christian Peest, J. Schmidt, R. Brendel, K. Bothe, M. R. Vogt, I. Kröger, S. Winter, A. Schirmacher, S. Lim, H. T. Nguyen, and D. MacDonald, "Uncertainty analysis for the coefficient of band-to-band absorption of crystalline silicon," AIP Adv. **5**(6), 067168 (2015).

[16] T. N. Nunley, N. S. Fernando, N. Samarasingha, J. M. Moya, C. M. Nelson, A. A. Medina, and S. Zollner, "Optical constants of germanium and thermally grown germanium dioxide from 0.5 to 6.6eV via a multisample ellipsometry investigation," J. Vac. Sci. Technol., B **34**(6), 061205 (2016).

[17] W. L. Bond, "Measurement of the refractive indices of several crystals," J. Appl. Phys. **36**(5), 1674 (1965).

[18] I. H. Malitson, "Interspecimen comparison of the refractive index of fused silica," J. Opt. Soc. Am. **55**(10), 1205–1209 (1965).

[19] Y. Yamamoto, P. Zaumseil, M. A. Schubert, and B. Tillack, "Influence of annealing conditions on threading dislocation density in Ge deposited on Si by reduced pressure chemical vapor deposition," Semicond. Sci. Technol. **33**(12), 124007 (2018).

[20] J. Schulze, A. Blech, A. Datta, I. A. Fischer, D. Hähnel, S. Naasz, E. Rolseth, and E.-M. Tropper, "Vertical Ge and GeSn heterojunction gate-all-around tunneling field effect transistors," Solid-State Electron. **110**, 59–64 (2015).

[21] L. Augel, J. Schlipf, S. Bullert, S. Bürzele, J. Schulze, and I. A. Fischer, "Photonic-plasmonic mode coupling in nanopillar Ge-on-Si PIN photodiodes," Sci. Rep. **11**(1), 5723 (2021).

[22] J. Kühne, J. Wang, T. Weber, L. Kühner, S. A. Maier, and A. Tittl, "Fabrication robustness in BIC metasurfaces," Nanophotonics **10**(17), 4305–4312 (2021).

[23] L. Augel, I. A. Fischer, M. Gollhofer, M. Oehme, and J. Schulze, "Comparing Fourier transform infrared spectroscopy results with photocurrent measurements for Ge-on-Si PIN photodetectors with and without Al nanoantennas," J. Appl. Phys. **128**(1), 013105 (2020).

[24] J. Schlipf and I. A. Fischer, "Rigorous coupled-wave analysis of a multi-layered plasmonic integrated refractive index sensor," Opt. Express **29**(22), 36201–36210 (2021).

[25] M. G. Moharam, E. B. Grann, D. A. Pommet, and T. K. Gaylord, "Formulation for stable and efficient implementation of the rigorous coupled-wave analysis of binary gratings," J. Opt. Soc. Am. A **12**(5), 1068–1076 (1995).

[26] J. Michel, J. Liu, and L. C. Kimerling, "High-performance Ge-on-Si photodetectors," Nat. Photonics **4**(8), 527–534 (2010).

[27] J. A. Nelder and R. Mead, "A simplex method for function minimization," Comput. J. **7**(4), 308–313 (1965).

[28] D. M. Kim, H. Zhang, H. Zhou, T. Du, Q. Wu, T. C. Mockler, and M. Y. Berezin, "Highly sensitive image-derived indices of water-stressed plants using hyperspectral imaging in SWIR and histogram analysis," Sci. Rep. **5**(1), 15919 (2015).

[29] G. Yu, G. Sapiro, and S. Mallat, "Solving inverse problems with piecewise linear estimators: From Gaussian mixture models to structured sparsity," IEEE Trans. Image Process. **21**(5), 2481–2499 (2012).

[30] A. Ribes and F. Schmitt, "Linear inverse problems in imaging," IEEE Signal Process. Mag. **25**(4), 84–99 (2008).